

# Evaluation of Hybrid Perovskite Prototypes After 10-Month Space Flight on the International Space Station

William Delmas, Samuel Erickson, Jorge Arteaga, Mark Woodall, Michael Scheibner, Timothy S. Krause, Kyle Crowley, Kaitlyn T. VanSant, Joseph M. Luther, Jennifer N. Williams, Jeremiah McNatt, Timothy J. Peshek, Lyndsey McMillon-Brown,\* and Sayantani Ghosh\*

Metal halide perovskites (MHPs) have emerged as a prominent new photovoltaic material combining a very competitive power conversion efficiency that rivals crystalline silicon with the added benefits of tunable properties for multijunction devices fabricated from solution which can yield high specific power. Perovskites have also demonstrated some of the lowest temperature coefficients and highest defect tolerance, which make them excellent candidates for aerospace applications. However, MHPs must demonstrate durability in space which presents different challenges than terrestrial operating environments. To decisively test the viability of perovskites being used in space, a perovskite thin film is positioned in low earth orbit for 10 months on the International Space Station, which was the first long-duration study of an MHP in space. Postflight high-resolution ultrafast spectroscopic characterization and comparison with control samples reveal that the flight sample exhibits superior photo-stability, no irreversible radiation damage, and a suppressed structural phase transition temperature by nearly 65 K, broadening the photovoltaic operational range. Further, significant photo-annealing of surface defects is shown following prolonged light-soaking postflight. These results emphasize that methylammonium lead iodide can be packaged adequately for space missions, affirming that space stressors can be managed as theorized.

are driven by human life support systems, scientific exploration and Earth observation equipment, telecommunications, and electric propulsion systems. There is great interest in highly efficient perovskite-structured thin-film solar cells for space applications.<sup>[1,2]</sup> These are promising candidates due to their excellent optoelectronic characteristics, low-cost, high performance,<sup>[2–4]</sup> and their facile manufacturability<sup>[5]</sup> potentially suitable for in-space manufacturing.<sup>[6]</sup> These traits coupled with their defect tolerance,<sup>[7,8]</sup> and radiation tolerance<sup>[9]</sup> have garnered interest for aerospace applications. Prior to the widespread implementation of metal halide perovskites (MHPs) into the space environment, solar cells must pass rigorous American Institute of Aeronautics and Astronautics Standard 111 (AIAA-S111) space qualification testing.<sup>[10]</sup> Low earth orbit (LEO), 160–2000 km above the Earth's surface, is an ideal place to operate MHPs either on the International Space Station or on satellites. The harsh environment of LEO includes thermal cycling ( $\pm 120$  °C), vacuum ( $10^{-6}$ – $10^{-9}$  torr), ultra-violet radiation, exposure to atomic oxygen (flux  $10^{13}$ – $10^{15}$

AO/cm<sup>2</sup> with collision energy of 5 eV), plasma ( $10^6$  cm<sup>-3</sup>,  $\leq 1$  eV electron temperature), and ionizing radiation of electrons, protons, micrometeoroids ( $60$  km s<sup>-1</sup>) and orbital debris ( $10$  km s<sup>-1</sup>).<sup>[11]</sup> We must demonstrate MHP durability in relevant space environments to evidence feasibility. Implementing


## 1. Introduction

As NASA readies technologies for Artemis missions with the goal of a sustained human presence on the moon, there is an increasing need for power. The expanding power requirements

W. Delmas, S. Erickson, J. Arteaga, M. Woodall, M. Scheibner, S. Ghosh  
Department of Physics  
University of California  
Merced, California 95343, USA  
E-mail: sghosh@ucmerced.edu  
T. S. Krause  
Universities Space Research Association  
National Aeronautics and Space Administration  
Cleveland, Ohio 44135, USA

K. Crowley, K. T. VanSant, J. McNatt, T. J. Peshek, L. McMillon-Brown  
Photovoltaic and Electrochemical Systems Branch  
John H. Glenn Research Center  
National Aeronautics and Space Administration  
Cleveland, Ohio 44135, USA  
E-mail: lyndsey.mcmillon-brown@nasa.gov  
J. M. Luther  
Materials, Chemical, and Computational Science Directorate  
National Renewable Energy Laboratory  
Golden, CO 80401, USA

J. N. Williams  
Department of Chemistry  
Wilberforce University  
Wilberforce, Ohio 45384, USA

 The ORCID identification number(s) for the author(s) of this article can be found under <https://doi.org/10.1002/aenm.202203920>.

DOI: 10.1002/aenm.202203920

MHPs in space<sup>[6]</sup> must be preceded by a systematic evaluation and understanding of long-term exposure to prevalent extreme conditions,<sup>[11]</sup> significantly different from those on Earth. Some investigations done in laboratory settings have indicated that MHPs are resistant to high-energy radiation<sup>[12–19]</sup> and to chemical instability under ultraviolet radiation in the absence of oxygen and moisture.<sup>[1,20]</sup> However, thermal cycling results in decreased PCE<sup>[21]</sup> and accelerated light-induced degradation in high vacuum.<sup>[22–24]</sup> This combination of results has not been clarified any further by the few prior forays of MHP devices into space.<sup>[20,19,24–26]</sup> Previous investigations have promising initial findings but have been limited to sub-orbital altitudes and very short flight times, on the order of hours to minutes. Additionally, as the samples investigated have been full devices, identifying the exact origin of the performance changes remains unknown.

We report the postflight analysis of perovskite thin films encapsulated using a space-grade, low-outgassing silicone after being flown on the International Space Station (ISS) as a part of the thirteenth Materials International Space Station Experiment (MISSE-13) and exposed to the space environment for 10 months, the longest space flight of MHPs to date. The sample was mounted on the Zenith position of the flight platform and exposed to the sun with the same orbital period as the ISS (90 min). Control samples were left on earth in a nitrogen-dry box. Unlike prior investigations, we have focused on the effect of prolonged space exposure on the MHP film alone, without the complication of charge transport layers and electrodes. Comparison of static and dynamic photoluminescence (PL) properties of both MISSE-13 (flight) and an identical control sample reveals a spectral blue-shift and increased charge recombination rate in the flight sample. Confocal imaging shows a higher density of surface defects in the flight film, which is likely a contributing factor in reducing the structural phase transition temperature<sup>[27]</sup> down to 56 K and enhancing the operational range.<sup>[28]</sup> However, under 15 h exposure to continuous AM1.5 illumination, the flight sample underwent extensive photo-healing, resulting in reduced surface defects and a nearly three-fold increase in carrier recombination lifetime, while simultaneously exhibiting excellent photostability.

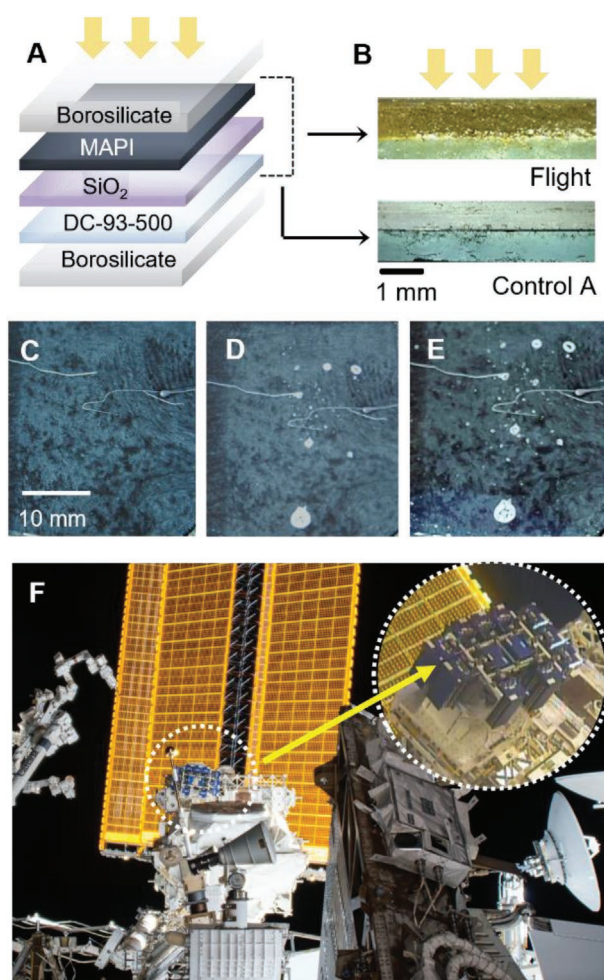


**Figure 1.** Flight sample pre- and postflight. A) Schematic of the sample stack. The MAPI film with a SiO<sub>2</sub> barrier layer is encapsulated with DC 93-500 and enclosed between borosilicate glass layers. B) Photographs of edges of (top) flight and (bottom) control A samples taken after the former's return. Bold arrows indicate the direction of illumination on the ISS. Photographs of flight sample C) preflight, immediately after fabrication, D) preflight, 290 h after fabrication, and E) postflight. F) ISS on day 52 of MISSE-13 duration. Yellow arrow highlights the position of the flight sample aboard the ISS.

## 2. Results and Discussion

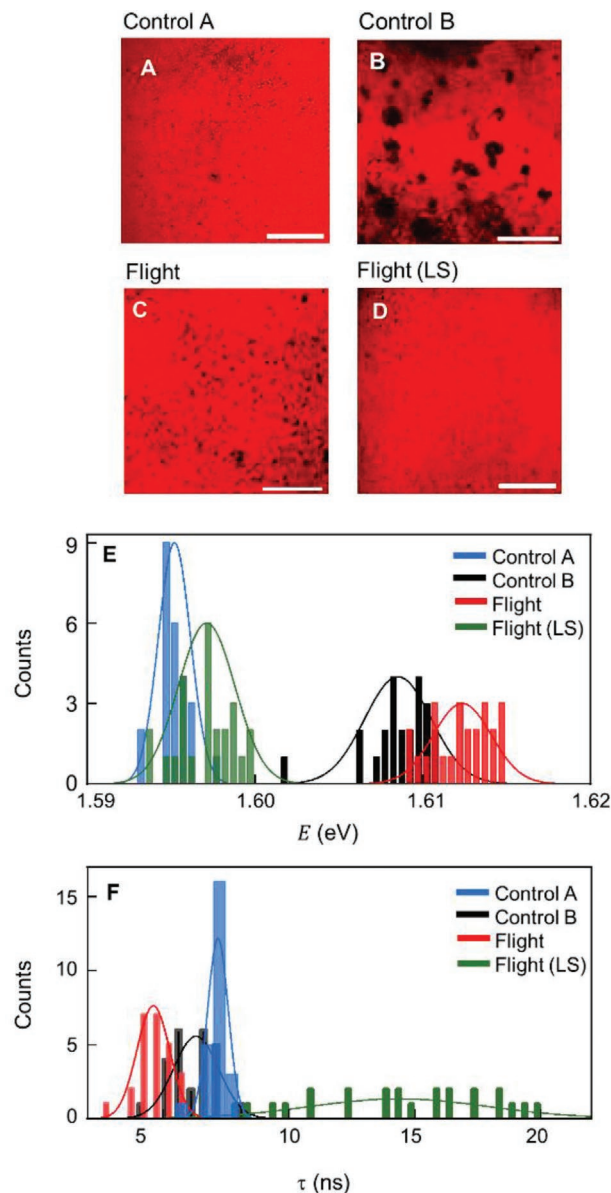
### 2.1. Optical Characterization

Figure 1A displays the composition of the stack used for both the MISSE-13 flight and control samples. A methylammonium lead iodide (CH<sub>3</sub>NH<sub>3</sub>PbI<sub>3</sub>, or MAPI) film was coated onto borosilicate glass, covered by a 50 nm layer of SiO<sub>2</sub>, followed by Dow-Corning space-grade encapsulant DC 93–500, a low outgassing silicone elastomer typically used to encapsulate electronics in aerospace applications. Another borosilicate slide is placed on the DC-93-500 during curing to complete the stack. Arrows in Figure 1A indicate the side of the sample that faced the sun on the ISS. Figure 1B shows side-view photographs of an identical control (control A) and the flight sample. The top glass layer of the latter (which faced the sun) shows yellowing, a typical signature of electron irradiation<sup>[14]</sup> in borosilicate glass. Ceria-doped borosilicates are radiation resistant and tend to be used for solar cell cover glasses.<sup>[28,29]</sup> In a desire to reduce weight these products tend to be 0.005 in. thick, which is challenging to use as a process substrate<sup>[30,31]</sup> therefore borosilicate glass was more readily sourced and suitable for MAPI deposition. A second sample (control B) with a similar architecture but without the SiO<sub>2</sub> layer was additionally monitored, and neither control shows any such changes (Figure S1, Supporting Information) to the substrates. In photographs of the flight sample taken prior to flight, immediately after synthesis (Figure 1C), and 290 h later (Figure 1D), we observe the formation of bubbles in the film. During this time the sample had been stored under ambient conditions, with the goal of assessing any obvious visual degradation. High-resolution imaging of the largest gap shows a bubble trapped within the encapsulant (Figure S2, Supporting Information). The area surrounding it

is nonemissive, implying degradation of the film driven by the moisture trapped within the bubble. However, this degradation is localized and not exacerbated significantly over the duration of the flight, as confirmed in Figure 1E, which was taken after the completion of the mission. The control samples did not suffer from the same problem.

## 2.2. Photoluminescence (PL) Spectroscopy

Fluorescence imaging via confocal microscopy in Figure 2 offers a comparison of the spatial uniformity of each sample, obtained via spectroscopy. Figure 2A–C are spatial maps of control A, control B, and the flight sample, respectively. All three show the varying distribution of regions that appear dark in this emission range (1.6 – 1.62 eV), yet they emit between 2.5 and 2.7 eV (Figure S3, Supporting Information), likely indicating that they are lead iodide (PbI<sub>2</sub>), a typical remnant of MAPI decomposition under the influence of moisture and oxygen.<sup>[32,33]</sup> The protective role played by the SiO<sub>2</sub> layer is clear in the comparison of Figure 2A,B. In the latter, 23% of the film surface shows this degradation, while the dark regions comprise just 4% of control A (Figure S4A, Supporting Information). However, the flight sample has ≈13% of its surface optically inactive (Figure S5A, Supporting Information), despite the passivation layer. To assess the effect of the difference in distribution of these dark spots, we spatially map (Figure S6A–D, Supporting Information) emission energy and charge recombination time over a 500 × 500 μm<sup>2</sup> area of all the films using scanning PL microscopy and summarize the results in Figure 2E,F. The first observation is the difference between the two controls, with emission energy *E* significantly blue-shifted in control B. Presence of PbI<sub>2</sub> within the MAPI microstructure has been known to have this effect.<sup>[34]</sup> However, while this may be true of control B, *E* is further blue-shifted in the flight sample, which has far fewer dark regions. The distribution of charge recombination lifetime  $\tau$ , measured over the same area and extracted from exponential fits to time-resolved PL data, follow a similar trend: recombination occurs faster on average in the flight sample than in either control. Taken together, these data indicate that the origin of emission energy and recombination rate variation in the flight sample is unlikely to be PbI<sub>2</sub> formation. A more plausible cause is the residual strain in the thin film that develops resultant of the rapid 4800 thermal cycles it underwent during its 10-month stint at the ISS. The thermal strain can be calculated as the temperature difference multiplied by the coefficient of thermal expansion difference between each layer ( $\epsilon_t = \Delta\alpha\Delta T$ ). The temperature change is referenced to the annealing temperature (100 °C), where residual strains are expected to be minimized. The thermal cycling is modeled by considering a uniform temperature plate exposed to sunlight in low Earth orbit on the top layer and thermally isolated at the bottom layer. The transient heat equation is then solved numerically to give a temperature profile throughout the orbit. Calculations reveal (Figure S7, Supporting Information) that over the time period of largest temperature decrease, MAPI experiences microscopic tensile strains in the *x* and *y*-directions, as the material is constrained by the thermal expansion mismatch with the glass and SiO<sub>2</sub> layers. Because of this constraint, the perovskite experiences



**Figure 2.** Comparisons of flight and control samples using static and dynamic spectroscopies. Confocal fluorescence images of A) control A, B) control B, and C) flight sample. D) Confocal fluorescence image of flight sample after 15 h light soaking (LS). Scale bars: 250 μm. Dark spots indicate regions of PbI<sub>2</sub> (Figure S3, Supporting Information). Distribution of (E) peak emission energy *E* and (F) Charge recombination lifetime  $\tau$  acquired from spatially resolved emission maps of flight and control samples (Figure S6, Supporting Information).

microscopic compressive strains in the *z*-direction due to the Poisson effect, whereas the corresponding strains in glass and SiO<sub>2</sub> are zero. The microscopic strain in the *z*-direction is computed as the product of twice the Poisson ratio and the thermal strain ( $\epsilon_{z, \text{micro}} = 2\nu\epsilon_t$ ). As the magnitude of the strains in the combined *x* and *y*-directions are larger than in the *z*-direction, the overall strain in the MAPI layer is expected to be largely tensile. At low temperatures, where the magnitudes are much higher, the resulting tensile strains could cause the valence

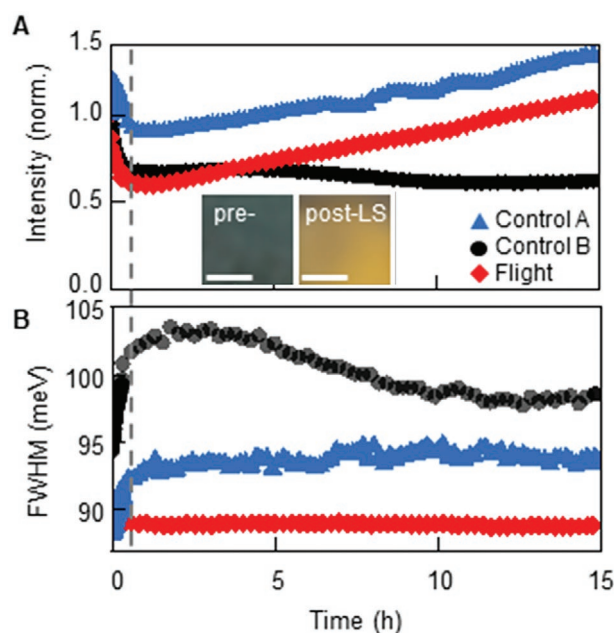


**Figure 3.** Evaluating the effect of flight on performance stability. A) Spectrally integrated PL intensity and B) Spectral full-width half maximum (FWHM) of PL emission monitored over time under continuous AM1.5 excitation, broadband and spectrally selected for flight and control samples. FWHM remains stable for the flight sample. Insets in (A) are photographs of control B before and after LS, showing extensive photo-induced degradation as evidenced by the color change from dark grey to yellow, signifying degradation of MAPI and formation of  $\text{PbI}_2$ .

band to move lower,<sup>[35]</sup> increasing the bandgap and causing spectral blue-shift.

### 2.3. Photostability

Following this initial characterization, the samples were exposed to AM1.5 solar radiation from a solar simulator while the spectral properties were monitored continuously. The effects of long-term light exposure on MHPs are complicated and vary based on fabrication method, composition of cations and halides, encapsulation properties, and duration of illumination.<sup>[36,37]</sup> The spectrally integrated PL intensities of controls A and B and the flight sample, normalized to the values at the onset, exhibit combinations of photodarkening and photobrightening in **Figure 3A**. Control A and the flight sample undergo an initial darkening, which is then followed by a gradual increase in emission intensity during the entire LS duration. Emission intensity of control B also decreases at the start, but does not recover. Current understanding of photo response of MHPs indicates both darkening and brightening begin immediately upon exposure to illumination and proceed simultaneously, with the dominant effect reflected in the observed data.<sup>[38]</sup> While photodarkening is a result of MAPI degrading into its constituent materials, increasing PL intensity can be driven by either passivation of trap states by photogenerated carriers, light-induced strain release, or a combination of both.<sup>[39,40]</sup> In **Figure 3B**, both control samples exhibit spectral broadening to varying

extents (higher in control B). The large increase in control B is due to MAPI degrading to  $\text{PbI}_2$  as the inset photographs confirm. While control A does not degrade as visibly (**Figure S4**, Supporting Information), the increase in spectral full width at half maximum (FWHM) attest to the formation of defect states driven by MAPI decomposition, which is also reflected in increased recombination rates after LS (**Figure S4C**, Supporting Information). The flight FWHM is highly stable, which again sets it apart from the other two. Light-induced lattice expansion has been known to cause strain relaxation, improving PCE and increasing emission intensity.<sup>[39]</sup> However, typically this is short-lived and inevitably followed by the expected chemical degradation. Not only is degradation not observed immediately after the light-soaking study in the flight sample, but confocal fluorescence imaging repeated after light-soaking (**Figure 2D**) shows reduced defect density on the film surface. The dark regions now account for only 6% of the film (**Figure S5B**, Supporting Information). By the end of LS, control B is entirely degraded and nonemissive, while control A shows no noticeable change (**Figure S4B**, Supporting Information). Repetition of spatially resolved emission and recombination map of the flight sample show not only a red-shifted emission from the film (**Figure 2E**) but a significant increase in charge lifetime (**Figure 2F**), on average three the mean  $\tau$  prior to light soaking. Both indicate extensive light-driven changes which are not observed in control A (**Figure S4C**, Supporting Information).

### 2.4. Temperature Dependent PL

This contrast between the samples extend to their behavior at low temperatures. Repeated and extreme thermal cycling is a consequence of any space mission, so it is essential that samples are stable under such conditions. MHPs undergo a structural transition from tetragonal to orthorhombic crystalline phase, which is in the range 140 – 160 K for MAPI and is accompanied by a change in the bandgap.<sup>[27]</sup> **Figure 4A** maps the PL emission intensity of control A as a function of temperature  $T$  and emission energy. At  $T = 120$  K, the emission energy shifts from 1.59 eV to 1.64 eV, indicating the transition to the higher energy crystalline phase, highlighted in **Figure 4D**. The spectral FWHM plotted in **Figure 4E** with temperature decreases steeply for  $T < T_C$ .  $T_C = 120$  K is lower than typical temperatures where this transition is observed, such as in control B, which exhibits a  $T_C = 148$  K (**Figure S8A**, Supporting Information), with accompanying changes to emission energy and FWHM in **Figure 4D,E**. We attribute the lower  $T_C$  in control A to the chemical vapor deposited  $\text{SiO}_2$  layer, since interfacial strain has been known to suppress the phase transition temperature in MAPI by up to 25 K.<sup>[41]</sup>

The same measurements for the flight sample show similar results in **Figure 4B, D**, and **E**, except the phase transition occurs at  $T_C = 56$  K. This is highly unusual, as the tetragonal phase is orientationally disordered and, therefore, as thermal vibrations are suppressed, gives way to the orthorhombic phase where the methylammonium ions are fully ordered. Prior instances where the crystal phase has been thermodynamically stabilized at temperatures lower than the transition have been in MHP nanocrystals.<sup>[42]</sup> The high surface-to-volume ratio in nanoscale structures results in the surface contributions to

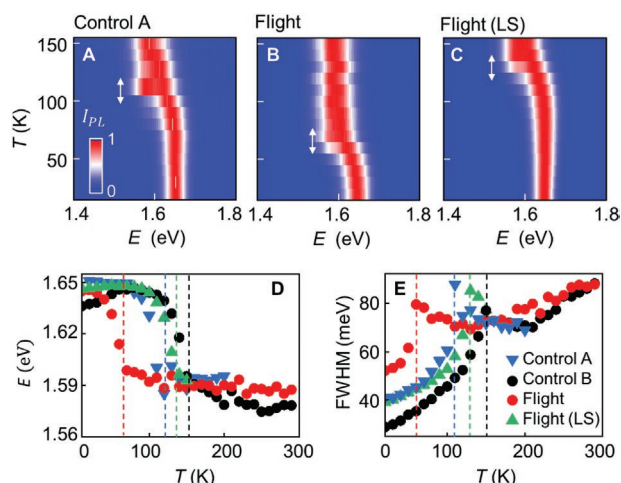


**Figure 4.** Structural phase transition. PL emission intensity mapped as functions of temperature  $T$  and emission energy  $E$  for A) control A and flight sample B) before and C) after light soaking (LS). The phase transition from tetragonal to orthorhombic crystalline structure occurs at  $T_C = 56$  K in the flight sample prior to LS.  $T_C$  after LS increases. D) Peak emission energy  $E$ , and E) FWHM of PL emission plotted with  $T$ . Dashed lines at  $T = T_C$  indicate flight and control samples have very similar low-temperature phase behavior except for the suppressed  $T_C$  of the former prior to light-soaking.

the Gibbs free energy significant enough that a different polymorph can dominate. The charge dynamics with temperature again underline clear differences between the two films. Time-resolved PL intensity  $I_{PL}$  at each  $T$  is fitted with bi-exponential fits  $I_{PL} = A_1 e^{-t/\tau_1} + A_2 e^{-t/\tau_2}$  and the fit parameters used to calculate an average charge lifetime  $\tau = [A_1\tau_1^2 + A_2\tau_2^2] / [A_1\tau_1 + A_2\tau_2]$ . A decreasing  $\tau$  is observed in both control samples (Figure S8B, Supporting Information) as  $T$  is lowered, indicating that recombination has excitonic contributions, confirmed by measuring the variation of  $I_{PL}$  with excitation power (Figure S9A, Supporting Information). Contrastingly,  $\tau$  is consistently shorter and almost entirely temperature independent in the flight sample. There is also a larger proportion of free carriers contributing to the recombination in the flight sample than in the control (Figure S9B, Supporting Information). Repeating these measurements after light soaking reveal additional impact of photo-annealing, where  $T_C$  of the flight sample increases to 130 K, close to the  $T_C$  of control A (Figure 4C-E), while the increased  $\tau$  observed in Figure 2F persists at low temperatures (Figure S8B, Supporting Information).

### 3. Conclusion

All the results thus far outline very encouraging consequences of exposing the MAPI film to space in low earth orbit. The flight sample is thermochemically stable. It displays a uniform emission energy and no indication of photodarkening or defect-induced spectral broadening for the entire 15 h duration of light soaking. Additionally, the transition to the orthorhombic phase is suppressed by nearly 65 K, which implies the temperature range over which the band gap, emission energy, charge carrier generation, and recombination properties remain stable

is broadened. The only potential drawback observed prior to light-soaking was the smaller lifetime  $\tau$  compared to the control samples. Charge lifetime is a good proxy for gauging photovoltaic performance. Short recombination times lead to charges recombining before arriving at the electrodes in the device stack, potentially reducing charge extraction efficiency, and thereby, open circuit voltage. Smaller  $\tau$  was most likely a result of the thermal cycling-induced strain, which was released with 15 h of light soaking, altering both the phase transition temperature and the recombination rates. Strain has been identified as the most significant factor in altering  $T_C$  in MAPI and inorganic halide perovskite films, where, either via lattice mismatch with substrates<sup>[41]</sup> or nano-engineering,<sup>[43]</sup> it has demonstrated the stabilization of specific structural phases. It is therefore likely that the flight sample strain allowed the tetragonal phase to stabilize thermodynamically, creating a unique segregated morphology where microcrystalline regions of both phases coexisted throughout the film with the lower band gap structure dominating recombination. As the sample photo-annealed, strain-release resulted in the charge lifetime increasing three-fold and the phase transition coming closer to the control sample. And although the lower  $T_C$  prior to light soaking was more desirable, the average lowest temperature at the lunar surface is  $\approx 140$  K, where the flight sample retains its tetragonal structure.

A few critical questions remain that require further investigation, one of which is the cause of the micro- or nano-scale strain in the flight sample. The repeated thermal cycling resulting from exposure to space might be introducing local minima in the energy landscape that activate cooler than usual, arising from a combination of defect creation and the resulting stress/strain. A recent study<sup>[21]</sup> demonstrated significant PL intensity loss and decreased lifetimes in an encapsulated MAPI film resulting from 200+ thermal cycles, caused by repeated structural phase transitions. The flight film undergoes a similar temperature cycle of 4800 times over the 10-month mission, indicating thermal cycling as a possible cause. Another candidate could be strain caused by defects induced by radiation, either UV, which is more intense on the ISS than on the earth's surface,<sup>[12]</sup> or ionizing radiation. The proton flux on the ISS is estimated to be  $10^9$  cm<sup>-2</sup> impacts over the 10-month period<sup>[44]</sup> with low energy protons (0.05–10 MeV) having higher fluence.<sup>[9,44]</sup> A close look at the photograph of the flight sample in Figure 1B shows that the interface between the glass slide and the encapsulant is considerably roughened compared to the control. Along with the yellowing of the glass, this is another possible evidence of radiation impact. However, SRIM (Stopping and Range of Ions in Matter) and TRIM (Transport of Ions in Matter) simulations (Figure S10, Supporting Information) show that protons with energy up to 15 MeV are stopped at the glass/encapsulant boundary, indicating that for this study radiation damage is unlikely to cause significant damage.<sup>[9]</sup> Regardless, while the radiation hardness of MHPs is well-documented,<sup>[12–19]</sup> this remains a topic that requires additional investigation using accurate stack architecture and testing guidelines.<sup>[9]</sup> Another issue is understanding the origin of the difference between the thermochemical stability of the two samples, and how that translates to their varied response to light soaking. With these questions in mind, we have prepared hybrid perovskite films and device stacks for the next mission (MISSE-15), which will provide additional answers.

Space flight of MHP on the MISSE platform is a valuable tool that affords the investigation of the combined effects of LEO environment. From this, we can glean in-situ performance and inform ground testing protocols. Through ground-based testing, researchers have observed temperature affects material properties and charge generation, transport, and recombination. Photovoltaic performance of devices decreases as temperature drops from 300 to 80 K.<sup>[28]</sup> The device attenuation at low temperature has been attributed to i) unbalanced charge transport in the device, ii) charge injection barrier at the electrode interface, and iii) charge separation barrier at the electron transport layer/perovskite interface.<sup>[45–49]</sup> Ground-based testing of perovskite degradation from ultra-high vacuum with illumination has been conducted.<sup>[50,51]</sup> However, methylammonium under a dark ultra-high vacuum did not exhibit similar degradation, suggesting that light is a key factor.<sup>[45]</sup> The material performance under vacuum will alter as the MHP is surrounded by other material layers in a device. Ground-based investigations of the impact of ultra-violet radiation-induced degradation demonstrate that performance can be managed with photon down-conversion or materials selection that slow UV-induced degradation.<sup>[52–54]</sup> Our flight sample has simultaneously experienced the aforementioned stressors, along with ionizing radiation and atomic oxygen. Understanding the contribution of each environmental factor on the MHP materials and devices will be of tremendous benefit beyond space PV applications in addressing the significant longevity challenges faced by MHP devices.

## 4. Experimental Section

**Sample Synthesis and Timeline:** All samples were fabricated at Case Western Reserve University in the MORE Lab User Facility in July 2019. The perovskite precursor solution was purchased from Sigma Aldrich and consisted of  $\text{CH}_3\text{NH}_3\text{I}$  and  $\text{PbI}_2$  in a 1:1 ratio dissolved at 40 wt.% in dimethylformamide (DMF). The encapsulant DC 93–500 is a silicone elastomer purchased from DOW CORNING and prepared by mixing the precursor with the hardening agent in a 10:1 ratio, stirring thoroughly, and then degassing at 40 °C in a vacuum oven. 30  $\mu\text{l}$  of the perovskite solution was drop cast onto glass substrates and spun at 2000 RPM for 90 s. The resulting MAPI film was annealed on a hotplate at 100 °C for 60 min. For the flight and control A samples, a 50 nm layer of  $\text{SiO}_2$  was deposited on top using an Angstrom Instruments Chemical Vapor Deposition system. For control B, all steps were identical except the  $\text{SiO}_2$  deposition. In October 2019, after humidity environment testing, samples were sent to Alpha Space Test and Research Alliance, LLC in Houston, TX, who has a contract with NASA to provide the MISSE flight facility (FF) services. The samples were integrated into the MISSE-FF, and then subjected to environmental testing. The environmental testing included a 3-axis vibration testing at 4.5 grms, and a high vacuum bakeout at 60 °C for 25 h. The samples were left in ambient conditions for  $\approx$ 5 months while preparing for space flight. The flight sample was launched aboard SpaceX Falcon on the 20<sup>th</sup> Commercial Resupply Mission (CRS-20) on March 7, 2020. Postlaunch, the control samples were returned to NASA Glenn for storage. On the ISS, the flight sample was mounted on the Zenith (sun-facing) position (Figure 1F) from March 2020 to January 2021,  $\approx$ 10-month period, and returned to Earth aboard SpaceX CRS-21, which landed on January 14, 2021. It was delivered to NASA Glenn  $\approx$ 2 months later. Data collection and analysis for all samples began in July 2021, two years after initial synthesis.

**Confocal Microscopy:** LSM 880 was used to take reflection and emission images of the flight and control samples. Samples were excited with a 405 nm laser. Reflection images of the samples were collected by

filtering light between 400 and 410 nm. Emission images were taken by filtering light between 750 and 800 nm.

**Photoluminescence (PL) Spectroscopy:** Samples were excited with a pulsed 532 nm laser light (NKT Photonics SuperK acousto-optic system) with a repetition rate of 39 MHz into an optical objective. Light emitted from the samples was filtered by a 650 nm long pass filter before reaching the spectrometer (Princeton Instruments Acton 2300) and single photon avalanche diode (SPAD, PicoQuant PDM series). The Gaussian PL profile was centered at 780 nm. The spectrometer head utilized a 500 nm blaze grating with 300 lines  $\text{mm}^{-1}$  to disperse the collected excitation into the CCD device. **PL Maps:** were taken with a 4x Olympus objective while the sample was translated with Newport 300 stages via a custom LabVIEW program. **Temperature Dependence:** The flight and control samples were loaded into a Montana Instruments cryostation for low-temperature measurements. While at a vacuum of 90  $\mu\text{Torr}$ , photoluminescence (PL) and time-resolved photoluminescence (TRPL) data were recorded every 10 K between 10 and 290 K. Along with PL and TRPL, photoluminescent excitation (PLE) and power dependent PL (PDPL) were recorded at 10 K and 200 K.

**AM1.5 Stability:** PL was measured every 5 min for 15 h under continuous illumination of a AM1.5 solar simulator (Newport LSH-7320 ABA LED Solar Simulator). The simulated sunlight was filtered with 675 nm short-pass filter before reaching the sample. Additionally, a 750 nm short pass filter was implemented in front of the sample in each test to filter infrared light that obscured the PL signal. A 675 nm long pass filter was used in the collection path in all tests to remove the effects of the solar simulator and record only light emitted from the sample. The PL signal was transmitted by fiber optic cable into an Acton 2300 spectrometer.

## Supporting Information

Supporting Information is available from the Wiley Online Library or from the author.

## Acknowledgements

W.D. and S.E. contributed equally to this work. The authors were grateful to the NASA Space Technology Mission Directorate for supporting this work through the following programs: The 2018 NASA Center Innovation Fund, and the NASA MIRO award no. NNX15AQ01A, and the 2019 Early Career Initiative. The authors also wish to extend gratitude to the state of Ohio's Third Frontier Program, the Case Western Reserve University Materials for Optoelectronics Research and Education Center, as well as the NASA Faculty Fellows Program, for the sample preparation and synthesis. The authors were also grateful to Alpha Space Test and Research 231 LLC (now, Aegis Aerospace) for providing the payload operations and for helpful discussions. This work was authored in part by the National Renewable Energy Laboratory, operated by Alliance for Sustainable Energy, LLC, for the U.S. Department of Energy (DOE) under Contract No. DE-AC36-08GO28308. The views expressed in the article do not necessarily represent the views of the DOE or the U.S. Government.

## Conflict of Interest

The authors declare no conflict of interest.

## Data Availability Statement

The data that support the findings of this study are available from the corresponding author upon reasonable request.

## Keywords

aerospace, International Space Station, light soaking, Metal halide perovskites, spectroscopy, strain, structural phase

Received: November 17, 2022

Revised: February 14, 2023

Published online:

- [1] V. Romano, A. Agresti, R. Verduci, G. D'Angelo, *ACS Energy Lett.* **2022**, *7*, 2490.
- [2] J. Yang, Q. Bao, L. Shen, L. Ding, *Nano Energy* **2020**, *76*, 105019.
- [3] Y. Tu, J. Wu, G. Xu, X. Yang, R. Cai, Q. Gong, *Adv. Mater.* **2021**, *33*, 2006545.
- [4] W. Yu, X. Sun, M. Xiao, T. Hou, X. Liu, B. Zheng, H. Yu, M. Zhang, Y. Huang, X. Hao, *Nano Res.* **2021**, *15*, 85.
- [5] Y. Vaynzof, Y. Vaynzof, *Adv. Energy Mater.* **2020**, *10*, 2003073.
- [6] L. McMillon-Brown, J. M. Luther, T. J. Peshek, *ACS Energy Lett.* **2022**, *7*, 1040.
- [7] T. Moot, J. B. Patel, G. McAndrews, E. J. Wolf, D. Morales, I. E. Gould, B. A. Rosales, C. C. Boyd, L. M. Wheeler, P. A. Parilla, S. W. Johnston, L. T. Schelhas, M. D. McGehee, J. M. Luther, *ACS Energy Lett.* **2021**, *6*, 2038.
- [8] G. W. Kim, A. Petrozza, *Adv. Energy Mater.* **2020**, *10*, 2001959.
- [9] A. R. Kirmani, B. K. Durant, J. Grandidier, N. M. Haegel, M. D. Kelzenberg, Y. M. Lao, M. D. McGehee, L. McMillon-Brown, D. P. Ostrowski, T. J. Peshek, B. Rout, I. R. Sellers, M. Steger, D. Walker, D. M. Wilt, K. T. VanSant, J. M. Luther, *Joule* **2022**, *6*, 1015.
- [10] M. M. Finckenor, K. K. de Groh, *A Researcher's Guide to: Space Environmental Effects*, NASA Johnson Space Center, Houston, Texas, USA **2020**.
- [11] R. Thirsk, A. Kuipers, C. Mukai, D. Williams, *CMAJ* **2009**, *180*, 1216.
- [12] G. M. Paternò, V. Robbiano, L. Santarelli, A. Zampetti, C. Cazzaniga, V. Garcia Sakai, F. Cacialli, *Sustainable Energy Fuels* **2019**, *3*, 2561.
- [13] Y. Miyazawa, M. Ikegami, T. Miyasaka, T. Ohshima, M. Imaizumi, K. Hirose, *IEEE Photovoltaic Spec. Conf. 42nd, IEEE*, New Orleans **2015**, p. 1.
- [14] Y. Miyazawa, I. Masashi, C. Hsin-Wei, O. Takeshi, I. Mitsuru, H. Kazuyuki, M. Tsutomu, *iScience* **2018**, *2*, 148.
- [15] B. K. Durant, H. Afshari, S. Singh, B. Rout, G. E. Eperon, I. R. Sellers, *ACS Energy Lett.* **2021**, *6*, 2362.
- [16] B. K. Durant, H. Afshari, S. Sourabh, V. Yeddub, M. T. Bamidele, S. Singh, B. Rout, G. E. Eperon, D. Y. Kim, I. R. Sellers, *Sol. Energy Mater. Sol. Cells* **2021**, *230*, 111232.
- [17] F. Lang, M. Jošt, J. Bundesmann, A. Denker, S. Albrecht, G. Landi, H. Neitzert, J. Rappich, N. H. Nickel, *Energy Environ. Sci.* **2019**, *12*, 1634.
- [18] F. Lang, M. Jošt, K. Frohna, E. Köhnen, A. Al-Ashouri, A. R. Bowman, T. Bertram, A. B. Morales-Vilches, D. Koushik, E. M. Tennyson, K. Galkowski, G. Landi, M. Creatore, B. Stannowski, C. A. Kaufmann, J. Bundesmann, J. Rappich, B. Rech, S. D. Stranks, *Joule* **2020**, *4*, 1054.
- [19] I. Cardinaletti, T. Vangerven, S. Nagels, R. Cornelissen, D. Schreurs, J. Hruby, J. Vodnik, D. Devisscher, J. Kesters, J. D'Haen, A. Franquet, V. Spampinato, T. Conard, W. Maes, W. Deferme, J. V. Manca, *Sol. Energy Mater. Sol. Cells* **2018**, *182*, 121.
- [20] J. He, T. Li, X. Liu, H. Su, Z. Ku, J. Zhong, F. Huang, Y. Peng, Y. Cheng, *Sol. Energy* **2019**, *188*, 312.
- [21] Y. Jiang, S. Yang, Q. Jeangros, S. Pisoni, T. Moser, S. Buecheler, A. N. Tiwari, F. Fu, *Joule* **2020**, *4*, 1087.
- [22] A. F. Akbulatov, M. I. Ustinova, G. V. Shilov, N. N. Dremova, I. S. Zhidkov, E. Z. Kurmaev, L. A. Frolova, A. F. Shestakov, S. M. Aldoshin, P. A. Troshin, *J. Phys. Chem. Lett.* **2021**, *12*, 4362.
- [23] G. Abdelmageed, C. Mackeen, K. a. Hellier, L. Jewell, L. Seymour, M. Tingwald, F. Bridges, J. Z. Zhang, S. Carter, *Sol. Energy Mater. Sol. Cells* **2017**, *174*, 566.
- [24] Y. Tu, G. Xu, X. Yang, Y. Zhang, Z. Li, R. Su, D. Luo, W. Yang, Y. Miao, R. Cai, L. Jiang, X. Du, Y. Yang, Q. Liu, Y. Gao, S. Zhao, W. Huang, Q. H. Gong, R. Zhu, *Sci. China, Ser. G: Phys., Mech. Astron.* **2019**, *62*, 974221.
- [25] L. K. Reb, M. Böhmer, B. Predeschly, S. Grott, C. L. Weindl, G. I. Ivandekic, R. Guo, C. Dreißigacker, R. Gernhäuser, A. Meyer, P. Müller-Buschbaum, *Joule* **2020**, *4*, 1880.
- [26] P. S. Whitfield, N. Herron, W. E. Guise, K. Page, Y. Q. Cheng, I. Milas, M. K. Crawford, *Stem Cells Int.* **2016**, *6*, 35685.
- [27] G. A. Haynes, *Effect of Radiation on Cerium-Doped Solar-Cell Cover Glass*, NASA Langley Technical Note D, XX **1970**, Vol. 6024.
- [28] H. Zhang, X. Qiao, Y. Shen, T. Moehl, S. M. Zakeeruddin, M. Grätzel, M. Wang, *J. Mater. Chem. A* **2015**, *3*, 11762.
- [29] a) D. B. Doyle, R. H. Czichy, in *Proc. SPIE*, **1994**, p. 434; b) D. B. Doyle, R. H. Czichy, presented at *Space Optics*, Garmisch, Germany **1994**.
- [30] T. D. Henson, G. K. Torrington, *Inorg. Opt. Mater. III* **2001**, *4452*, 54.
- [31] S. F. Pellcori, C. L. Martinez, P. Hausgen, D. Wilt, *Appl. Opt.* **2014**, *53*, A339.
- [32] W. Tress, K. Domanski, B. Carlsen, A. Agarwalla, E. A. Alharbi, M. Graetzel, A. Hagfeldt, *Nat. Energy* **2019**, *4*, 568.
- [33] B. R. Ecker, C. Wang, H. Wei, Y. Yuan, J. Huang, Y. Gao, *Adv. Mater. Interfaces* **2018**, *5*, 1801206.
- [34] H. Choi, J. C. Ke, S. Skalsky, C. A. Castle, K. Li, K. L. Moore, W. R. Flavell, P. Parkinson, *J. Mater. Chem. C* **2020**, *8*, 7509.
- [35] C. Zhu, X. Niu, Y. Fu, N. Li, C. Hu, Y. Chen, X. He, G. Na, P. Liu, H. Zai, Y. Ge, Y. Lu, X. Ke, Y. Bai, S. Yang, P. Chen, Y. Li, M. Sui, L. Zhang, H. Zhou, Q. Chen, *Nat. Commun.* **2019**, *10*, 815.
- [36] S. Kundu, T. L. Kelly, *EcoMat* **2020**, *2*, e12025.
- [37] C. C. Boyd, R. Cheacharoen, T. Leijtens, M. D. McGehee, *Chem. Rev.* **2018**, *119*, 3418.
- [38] E. V. Péan, C. S. De Castro, M. L. Davies, *Mater. Lett.* **2019**, *243*, 191.
- [39] X. Fu, D. A. Jacobs, F. J. Beck, T. Duong, H. Shen, K. R. Catchpole, T. P. White, *Phys. Chem. Chem. Phys.* **2016**, *18*, 22557.
- [40] H. Tsai, R. Asadpour, J. Blancon, C. C. Stoumpos, O. Durand, J. W. Strzalka, B. Chen, R. Verduzco, P. M. Ajayan, S. Tretiak, J. Even, M. A. Alam, M. G. Kanatzidis, W. Nie, A. D. Mohite, *Science* **2018**, *360*, 67.
- [41] S. A. Shojaee, T. A. Harriman, G. S. Han, J. K. Lee, D. A. Lucca, *Appl. Phys. Lett.* **2017**, *111*, 023902.
- [42] W. G. Delmas, E. T. Vickers, A. C. DiBenedetto, C. Lum, I. N. Hernandez, J. Z. Zhang, S. Ghosh, *J. Phys. Chem. Lett.* **2020**, *11*, 7886.
- [43] S. Ma, S. H. Kim, B. Jeong, H. Kwon, S. Yun, G. Jang, H. Yang, C. Park, D. Lee, J. Moon, *Small* **2019**, *15*, 1900219.
- [44] E. R. Benton, E. V. Benton, *Nucl. Instrum. Methods Phys. Res. Sect. B* **2001**, *184*, 255.
- [45] Y. Tu, J. Wu, G. Xu, X. Yang, R. Cai, Q. Gong, R. Zhu, W. Huang, *Adv. Mater.* **2021**, *33*, 2006545.
- [46] T. J. Jacobsson, W. Tress, J. Correa-Baena, T. Edvinsson, A. Hagfeldt, *J. Phys. Chem. C* **2016**, *120*, 11382.
- [47] S. Shao, J. Liu, H. Fang, L. Qiu, G. H. ten Brink, J. C. Hummelen, L. J. A. Koster, M. A. Loi, *Adv. Energy Mater.* **2017**, *7*, 1701305.
- [48] G. Liu, C. Zhou, F. Wan, K. Li, Y. Yuan, Y. Gao, Y. Lu, B. Yang, *Appl. Phys. Lett.* **2018**, *113*, 113501.
- [49] N. Shrestha, Z. Song, C. Chen, E. Bastola, X. Wang, Y. Yan, R. J. Ellingson, *J. Phys. Chem. Lett.* **2020**, *11*, 121.
- [50] J. Xiao, L. Liu, D. Zhang, N. De Marco, J. Lee, O. Lin, Q. Chen, Y. Yang, *Adv. Energy Mater.* **2017**, *7*, 1700491.
- [51] C. Yi, J. Luo, S. Meloni, A. Boziki, N. Ashari-Astani, C. Grätzel, S. M. Zakeeruddin, U. Röhthlisberger, M. Grätzel, *Energy Environ. Sci.* **2016**, *9*, 656.
- [52] F. Bella, G. Griffini, J. Correa-Baena, G. Saracco, M. Grätzel, A. Hagfeldt, S. Turri, C. Gerbaldi, *Science* **2016**, *354*, 203.
- [53] H. Roh, G. S. Han, S. Lee, S. Kim, S. Choi, C. Yoon, J. Lee, *J. Power Sources* **2018**, *389*, 135.
- [54] S. S. Shin, E. J. Yeom, W. S. Yang, S. Hur, M. G. Kim, J. Im, J. Seo, J. H. Noh, S. I. Seok, *Science* **2017**, *356*, 167.